Combined electron energy-loss and cathodoluminescence spectroscopy on individual and composite plasmonic nanostructures

Toon Coenen,[1] David T. Schoen,[2] Benjamin J. M. Brenny,[1] Albert Polman,[1] and Mark L. Brongersma[2,*]

[1]*Center for Nanophotonics, FOM Institute AMOLF, Science Park 104, 1098 XG Amsterdam, The Netherlands*
[2]*Geballe Laboratory for Advanced Materials, Stanford University, Stanford, California 94305, USA*

We systematically investigate the plasmonic "dolmen" geometry and its constituent elements using electron energy-loss spectroscopy and cathodoluminescence spectroscopy. In particular, we study the effects of the particle size and spacing on the resonant behavior and interparticle coupling. Because we apply both techniques on the same structures we can directly compare the results and investigate the radiative versus nonradiative character of the different modes. We find that the cathodoluminescence response is significantly lower than the electron energy-loss response for higher-energy modes because strong absorption reduces the scattering efficiency in this regime. Furthermore, we show that the overall resonant response roughly scales with size as expected for plasmonic structures but that the transverse resonant modes do become more dominant in larger structures due to a relative reduction in Ohmic dissipation. Using EELS and CL we can rigorously study coupling between the elements and show that the coupling diminishes for larger spacings.

I. INTRODUCTION

In the field of nanophotonics, metallic and high-index dielectric building blocks are used to confine, modulate, and steer light at the nanoscale [1–5]. To resolve and understand these optical processes there is a need for high-resolution optical spectroscopy techniques. Electron beam spectroscopy techniques [6], such as cathodoluminescence (CL) spectroscopy [7–11] and electron energy-loss spectroscopy (EELS) [12–19] have gained significant interest recently because they combine the ultrahigh spatial resolution from electron microscopes with broadband optical sensitivity. In CL spectroscopy one collects the light that is emitted after electron beam excitation, whereas in EELS the energy loss of the electrons is probed in an electron spectrometer. Scanning-transmission electron microscopy (STEM) EELS is performed in a transmission electron microscope (TEM) and hence requires electron-transparent samples in which inelastic electron scattering is minimized. In EELS one can benefit from the very fine electron probe, which allows precise characterization of the sample geometry [20] and composition down to the atomic level [21]. CL spectroscopy is typically performed in a scanning electron microscope (SEM) although CL collection systems have also been successfully implemented in TEMs [8,22]. SEMs are easier to operate and allow experiments to be performed on thick samples but the electron probe is larger in size. While both experimental techniques have their advantages and disadvantages they have proven to be very useful for studying optical processes at the nanoscale. In fact, because the techniques measure different quantities, they are complementary. The EELS response includes radiative and nonradiative processes, whereas CL spectroscopy solely probes radiative processes [6,23]. Combining these two techniques can thus provide additional information on optical modes in nanostructures, e.g., whether modes are "dark" or "bright" in nature. Here, we combine these electron beam techniques to elucidate the nanoscale optical properties of the plasmonic dolmen structure and its constituent components; a horizontally oriented single bar and a vertically oriented dimer structure [24–31]. We study the properties of these individual components in detail. Subsequently, we examine the complete dolmen geometry, specifically the effect of element size and their separation on the total response. We interpret the experimental results by comparing them to full-wave finite-difference time-domain (FDTD) simulations [32]. These experiments provide detailed insight into the radiative versus nonradiative character of nanoscale optical modes and show the strength of combining CL and EELS spectroscopy in such experiments.

II. EXPERIMENTAL METHODS

We fabricated plasmonic dolmens of three different sizes (see Table I for exact dimensions) and corresponding reference structures on electron-transparent 15-nm-thick Si_3N_4 membranes using a combination of electron beam lithography, thermal evaporation, and liftoff (see Ref. [33] for a detailed description of the fabrication procedures). Figure 1 shows bright-field transmission electron micrographs of the three dolmen structures under investigation. In (a) we have included the relevant regions of interest **A**, **B** and the characteristic dimensions describing the dolmen geometry. Although we have drawn only one box per region of interest, we have used two (on the left and right side of the structure), making use of the symmetry of the dolmen to improve the signal-to-noise ratio in the spectra. This averaging does not significantly affect the overall spectral shape.

The CL measurements were performed in a FEI XL-30 SFEG SEM equipped with a home-built CL system [7,34]. The measurements were taken using a 30-kV acceleration voltage and a beam current of 0.8 nA. The pixel sizes were 7.5, 8.5, and 10 nm for the three dolmen sizes, respectively, with an integration time of 0.5 s per pixel. The EELS measurements were taken in a monochromated FEI Titan TEM in scanning

*Corresponding author: brongersma@stanford.edu

TABLE I. Dimensions of the dolmen structures for the three different sizes. The in-plane dimensions were derived from BF TEM data and the thickness from atomic force microscopy (AFM) measurements on reference metal pads on the membrane support. The dimensions are listed in nanometers.

	$L1$	$W1$	$L2$	$W2$	S	d	h
Size 1	125	60	90	40	30	30–60	33
Size 2	185	85	130	60	40	45	40
Size 3	215	100	160	90	30	45	40

transmission electron microscopy (STEM) mode at 300-kV acceleration voltage with a beam current of 0.2 nA. During the EELS acquisition we simultaneously collect a STEM image using the annular dark-field detector. To obtain a good reference spectrum we measure the zero-loss peak (ZLP) through a punctured membrane, i.e., through vacuum. From this measurement we determined that the energy spread of the primary beam was 80 meV (full width at half maximum). We use a Richardson-Lucy algorithm to deconvolute the experimental EELS spectra with the ZLP, which is considered to represent the point spread function (PSF) of the system in energy space. The scanning pixel sizes were 3, 3.75, and 5 nm for the three dolmen sizes, respectively, with an integration time of 5 ms per pixel. We convert the EELS data to intensity

per unit wavelength by applying the appropriate Jacobian $(hc/e\lambda_0^2)$. This allows us to directly compare the spectral shapes obtained in EELS and CL. In order to quantitatively compare the absolute EELS and CL signals, one would need to account for the beam currents, integration times, and absolute system responses, which are challenging to determine exactly. Additionally, the experiments were performed at different acceleration voltages, which has an effect on the plasmon excitation probability [6]. Hence, we show normalized spectra, which allow direct comparison of the spectral shape but cannot be used for quantitative comparison. The EELS experiments were performed before the CL experiments in this case.

III. SINGLE NANORODS AND DIMERS

In order to understand the response of the dolmen structure under electron beam irradiation we first study the response of its constituent building blocks. To that end we measured spatially resolved CL and EELS spectra on individual rods and dimers. We raster-scan the electron beam in small steps over the structure and measure the EELS/CL spectrum at each position. As the gold layer is quite thick (~40 nm as determined with AFM), the EELS signal that is measured through the metal does not uniquely represent the optical resonances as other inelastic processes occurring in the dense gold layer also cause energy loss. We therefore only
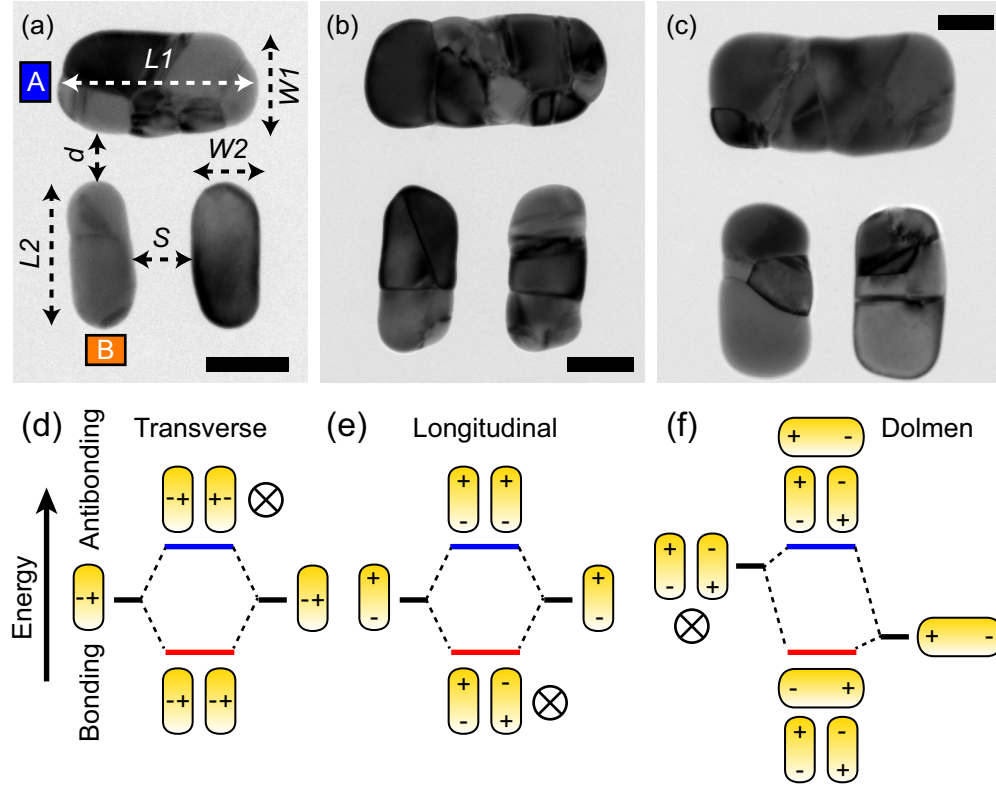

FIG. 1. Bright-field transmission electron micrographs of the dolmen structures with (a) size 1, (b) size 2, and (c) size 3. In (a) we have also indicated the relevant regions of interest for the experiment (**A**, **B**) and the characteristic dimensions of the dolmen structure. Scale bars correspond to 50 nm. Hybridization schemes for (d) transverse dimer modes, (e) longitudinal dimer modes, and (f) relevant dolmen modes. Each set of resonances hybridizes to give a set of bonding (lower energy) and antibonding modes (higher energy). In the case of the dolmen the hybridizing bare-state resonances are also detuned in frequency, which leads to asymmetric mode splitting. The $\otimes$ symbol indicates that a mode is symmetry forbidden for plane-wave excitation at normal incidence.
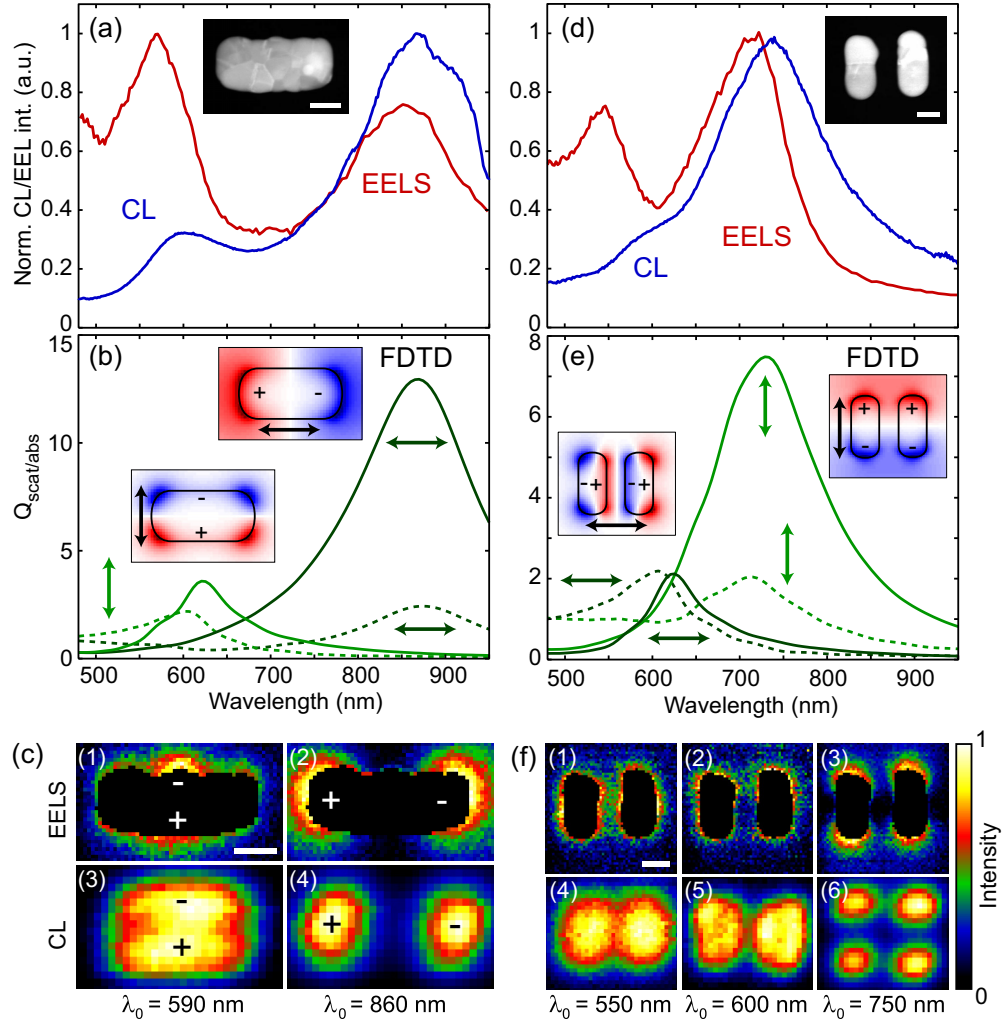
FIG. 2. CL and EELS spectra, spatially integrated over the full scan area of (a) a single gold rod and (d) a dimer with similar dimensions to the size 2 dolmen. The peak amplitudes and positions are listed in Table II. ADF STEM images of the structures are shown as insets. (b, e) Scattering (solid curves) and absorption (dashed curves) cross-section simulations for the single bar and dimer for two orthogonal polarizations as indicated by the arrows, calculated using a TFSF source in FDTD. The cross sections have been normalized by the geometrical cross sections of the structures. As insets we show the corresponding E_z near-field distributions. (c) EELS and CL spatial excitation distributions for the single rod for $\lambda_0 = 590$ and 860 nm corresponding to transverse and longitudinal dipole resonances. (f) EELS and CL spatial excitation distributions for the dimer for $\lambda_0 = 550$, 600, and 750 nm. Scale bars correspond to 50 nm.

take into account the excitation positions where the beam does not directly hit the structure. Because the evanescent electromagnetic fields extend away from the electron trajectory it can still couple to the nanostructure in this "aloof" excitation configuration, while it does not experience inelastic collisions in the dense gold material.

Figure 2(a) shows the CL and EELS spectra for a single gold rod with dimensions corresponding to dolmen size 2, spatially integrated over the full scan area. An annular dark-field (ADF) STEM image of the structure is shown as inset. We clearly observe two peaks in the spectra, which correspond to localized surface plasmon resonances (LSPRs) in the structure (see Table II for peak positions and amplitudes). To identify these resonances we simulate the scattering (Q_{scat}) and absorption (Q_{abs}) cross sections (normalized to the geometrical cross section) for plane-wave excitation with the polarization along and transverse to the long axis of the rod, using total-field scattered-field simulations in FDTD [32] (for details on the

simulation setups see supplementary information in Ref. [33]). Although plane-wave excitation is physically different from electron beam excitation, such simulations still provide a straightforward tool to identify relevant modes and to quantify their radiative and absorptive extinction. While this approach is fast and simple and the method of choice in this case, we note

TABLE II. Peak amplitudes and center wavelengths (in between brackets) of the normalized CL and EELS spectra for the monomer [Fig. 2(a)] and dimer [Fig. 2(d)]. The modes are numbered going from blue to red for both the monomer and dimer.

	CL	EELS
Monomer peak 1	0.32 (598 nm)	1 (566 nm)
Monomer peak 2	1 (867 nm)	0.78 (855 nm)
Dimer peak 1	0.31 (584 nm)	0.69 (541 nm)
Dimer peak 2	1 (740 nm)	1 (720 nm)

that rigorous 3D simulation methods could be employed as well, such as the green dyadic method [35], the discontinuous Galerkin method [36], the boundary-element method [37,38], electron-driven discrete-dipole approximation [39], or line-dipole FDTD simulations [40]. These approaches can be more directly compared to EELS and CL experiments because they can include the electron beam interaction with the structure and hence they can provide a means to obtain even more direct quantitative insight into the radiative and nonradiative properties of nanophotonic structures.

The simulation results are shown in Fig. 2(b). For polarization along the long axis we observe a peak in the scattering at $\lambda_0 = 860$ nm while for transverse polarization a peak is observed at $\lambda_0 = 620$ nm. Both resonances have cross sections that significantly exceed the geometrical cross section of the particle, as is often the case for LSPRs. The transverse resonance is blueshifted with respect to the longitudinal resonance because the conduction electrons experience a larger restoring force due to the reduced width. As insets we also plot the real part of the out-of-plane electric field component (E_z) of the induced near-field (in the middle of the rod, $h = 20$ nm), which clearly reveals that we are driving transverse (high-energy peak) and longitudinal (low-energy peak) electric dipole resonances. In the FDTD field map for the transverse mode we observe four spots in which the fields are higher, whereas this is not the case in the actual experiment. We attribute this to the fact that the real structures are more rounded than the simulated structures, mitigating these hotspot effects.

The simulated scattering cross section spectrum qualitatively matches the integrated CL data, where the resonance wavelengths, linewidths, and relative peak heights are well-reproduced. This is expected as CL probes the radiative response only [6,23]. While the EELS spectrum shows similar peak wavelengths and linewidths, the transverse resonance is stronger than the longitudinal resonance (see also Table II), contrary to the CL measurement. This can be explained as follows: The transverse dipole mode is strongly confined to the rod and hence a significant amount of the field resides within the metal. Additionally, the resonance wavelength is in a spectral regime where gold is absorbing significantly due to interband transitions. As a result, Ohmic dissipation is significant for the transverse mode and the scattering is rather weak, as illustrated by the low peak amplitude in CL. Because the absorption is strong for this mode the total extinction, i.e., the sum of absorption and scattering, is significantly larger than the purely radiative scattering response. In Fig. 2(b) the simulated total extinction for the two polarizations can be obtained by summing the solid and dashed curves. As the total extinction corresponds to the quantity that is measured with EELS, a larger peak amplitude is expected compared to CL, consistent with the data. In contrast, for the longitudinal mode the degree of confinement is smaller and gold is also less absorbing in the IR. Hence, the structure scatters more efficiently at this wavelength, leading to a strong peak in CL compared to the transverse mode. These observations are corroborated by the FDTD simulations.

We note that for the transverse resonance the CL and EELS data are slightly blueshifted compared to the FDTD results. It has been suggested that one might expect a redshift in the EELS measurement, compared to an optical experiment because the near-field should be redshifted compared to the far-field [41]. Thus far it has not been resolved in literature whether CL and EELS measurements are generally blueshifted or redshifted with respect to each other or compared to optical data and it highly depends on the experiment and structure what is observed [42,43]. For comparison with optical simulations, differences in the exact sample geometry and optical constants are a major factor but there are several other effects as well that can influence the experimentally measured spectral positions such as charging and carbon deposition as is explained in detail in Ref. [43].

By studying the spatial EELS and CL profiles we can verify the nature of the observed resonance peaks. Figure 2(c) shows the 2D EELS and CL excitation maps at two resonance wavelengths. As the electron beam preferentially couples to E_z components [6], an electrical dipole resonance will be excited efficiently at the particle extremities along the dipole axis, as there is a strong E_z component at those positions [see the field profiles in Fig. 2(b)] [44,45]. Indeed, the EELS and CL maps clearly show such features, consistent with the excitation of in-plane transverse and longitudinal dipole resonances.

Next, we perform a similar analysis for the isolated dimer structure. The response of a single dimer rod is not shown here as it is similar to what is shown in Figs. 2(a)–2(c) but blueshifted because of the smaller rod size. Figure 2(d) shows the spatially integrated CL and EELS spectra for the dimer. Again, two peaks are clearly visible in the spectra. The short-wavelength peak is quite weak for CL and appears as a shoulder around $\lambda_0 = 600$ nm, whereas for EELS it is much more pronounced and centered around $\lambda_0 = 550$ nm. The FDTD field plots in the inset of (e) shows that plane-wave excitation drives transverse and longitudinal dipole modes with the rods excited in phase. Compared to a single dimer rod, however, these collective dimer modes are redshifted for the transverse mode and blueshifted for the longitudinal mode, respectively (not shown here). This can be understood from a hybridization scheme where the transverse mode is energetically favorable (bonding) and the longitudinal mode is energetically unfavorable (antibonding) due to the charge distributions associated with these modes [see Figs. 1(d) and 1(e)] [46,47]. For the dimer it is less straightforward to directly compare the plane-wave case to the CL and EELS spectra and excitation maps as we could for the single rod. The dimer also supports an antibonding mode for transverse excitation and a bonding mode for longitudinal excitation, where the dipole moments in the rods are in antiphase [again, see hybridization schemes in Figs. 1(d) and 1(e)]. These modes are symmetry-forbidden for plane-wave excitation under normal incidence [48–51] but can be accessed with local electron beam excitation [39,44,52–54]. Hence, the peaks observed in CL and EELS could be due to four modes rather than two.

We can use the spatial profiles in Fig. 2(f) to help with the identification of the peaks observed in the EELS and CL data. For the blue peak in EELS at $\lambda_0 = 550$ nm (excitation map 1) we observe excitation hotspots along the short axis of the rods and a relatively high excitation probability in the gap region between the two rods, whereas at $\lambda_0 = 600$ nm (excitation map 2) the excitation probability is significantly lower in the gap region. In the transverse bonding mode
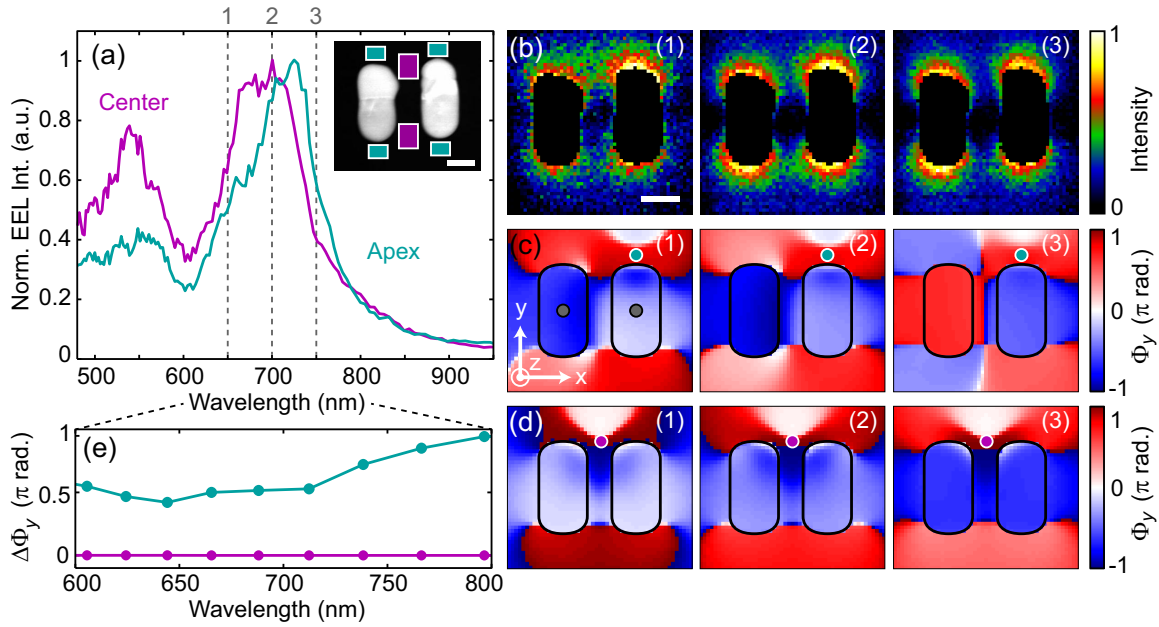
FIG. 3. EELS spectra taken at the apices (cyan curve) and in the center (magenta curves) of the size 2 dimer. The spectral collection areas are indicated in the STEM image (inset). (b) EELS excitation maps taken at $\lambda_0 = 650$, 700, and 750 nm (maps 1–3), respectively, as indicated by the dashed lines in (a). (c) E_y near-field phase distributions of the dimer from FDTD when excited by a vertical point dipole source 10 nm away from the apex of the right rod. The results are plotted for $\lambda_0 = 665$, 710, and 765 nm and are taken at half-height of the structure. For reference the coordinate system is indicated. (d) Same plot as in (c) but now for excitation in between the rods. (e) Phase difference in E_y between center positions in the rods, calculated from the fields in (c) and (d) and plotted for the relevant spectral range ($\lambda_0 = 600$–800 nm). The center positions are indicated by the gray dots in map 1 in (c). Scale bars are 50 nm.

destructive interference leads to near-zero E_z component in the center of the gap [clearly visible in the E_z field profile for this mode in Fig. 2(e)], so a low excitability is expected at that position. In contrast, for the transverse antibonding mode there is constructive E_z interference leading to a high excitability in the gap region [44,52–54]. We therefore conclude that map 1 is consistent with the transverse antibonding mode and map 2 is consistent with the transverse bonding dimer mode. The position of the peak in CL coincides with the peak in FDTD for the bonding mode and also the spatial profile matches well with the calculated field profile for that mode [see Fig. 1(e)]. The blueshifted antibonding mode does not radiate efficiently, which is most likely caused by strong absorption and destructive interference in the far field. Hence, its contribution to CL is small compared to the EELS spectrum. We note that the vertical z-dipole mode in the rods could play a role in explaining the discrepancy between the EELS and CL signal as well. This resonance has a low albedo due to the high degree of confinement along the z axis, and thus may appear more clearly in the EELS spectrum. FDTD simulations show that this resonance peaks around $\lambda_0 = 500$ nm with a maximum extinction cross section of 1.6 (not shown). Finally, we note that gold can also show material-related energy losses in the blue part of the spectrum as a result of interband transitions and bulk plasmons, but these are mostly filtered out by only considering aloof electron trajectories.

We will now focus on the longitudinal dimer modes, which are dominant in this geometry and most relevant for the canonical dolmen modes discussed in literature [24–26,33]. In principle, when the two rods are brought close enough the

longitudinal bonding and antibonding modes can split in energy such that separate peaks are visible [49]. However, in our case it is not possible to attribute the resonant peak at $\lambda_0 = 750$ in Fig. 2(d) to a mode from the spectrum alone because there is no observable splitting. In our configuration, the apices where the fields are strongest are relatively far apart, resulting in small field overlap and coupling, making the bonding and antibonding mode close to degenerate in energy. Again, using the spatially resolved spectral information provided by EELS and CL aids the interpretation of the observed spectral feature.

The EELS and CL maps of the dimer for the peak at $\lambda_0 = 750$ nm [maps 3 and 6 in Fig. 2(f)] show that the excitation probability is highest at the rod apices but such behavior is expected for both the bonding and antibonding longitudinal modes. However, there should be a subtle difference between the two modes. For the antibonding mode the rods are in phase leading to constructive E_z interference in the gap region near the apices [also clear in the E_z profile for this mode in Fig. 2(e)]. As a consequence we expect that this mode can be efficiently driven in the gap region as well, whereas for the bonding mode that is not possible because there is no E_z component present due to destructive interference. In our case the maps are more consistent with the latter case. Figure 3 shows the EELS spectra for excitation within the gap and at the apices, which clearly show a redshift of the spectrum for the apices compared to within the gap. This effect is also apparent in the spatial EELS profiles in the range $\lambda_0 = 650$ to 750 nm, where the gap region gradually becomes darker for increasing wavelength [see maps 1–3 in Fig. 3(b)]. These observations suggest that the main peak at $\lambda_0 = 750$ nm in

the spatially averaged spectrum in Fig. 2(d) is due to two modes, where the excitation efficiency strongly depends on the excitation position and wavelength; the excitation efficiency of the antibonding mode decreases relative to the bonding mode for increasing wavelength.

To verify this hypothesis we perform FDTD simulations in a similar setup as in Ref. [33], where we place a vertically oriented electrical point-dipole source as an approximation for the electron beam excitation at two positions: at the apex of one of the dimer rods and in between the rods, similar to the excitation areas for the spectra shown in Fig. 3(a). The driving field of the dipole cannot be removed like we could for plane-wave excitation and as a result the simulations show a mix of the driving field and the induced field on the dimer. To mitigate the obscuring effect of the driving fields we look at the E_y field component rather than at the E_z component, which is very strongly present in the driving field due to the vertical orientation of the driving dipole. Furthermore, by comparing the phase of E_y (Φ_y) in the two rod centers we can straightforwardly determine whether the rods are in or out of phase, i.e., in the antibonding or bonding modal configuration. Figures 3(c) and 3(d) show 2D Φ_y maps for excitation at the apex and in between the rods like in Fig. 3(a), for $\lambda_0 = 665$, 710, and 765 nm. The patterns are taken at half-height of the structure. Although most of the driving field is filtered out by only considering E_y, there is still some residual asymmetry visible, but this should not significantly affect the interpretation of the phase distribution. Clearly, there is a substantial phase difference between the rods for excitation at the apex, whereas for excitation between the rods the phase is equal as expected from symmetry. These trends are quantified in Fig. 3(e), where we have plotted the phase difference ($\Delta\Phi_y$) for the two excitation positions in the relevant spectral region ($\lambda_0 = 600$–800 nm). For excitation in the center the phase difference is 0, but for the apex excitation the phase difference is nonzero and goes from being 0.5π to π for $\lambda_0 = 800$ nm. This suggests that at the center, the symmetric antibonding mode is predominantly excited, whereas a mixture of the the two modes is excited at the apices, with the contribution of the antisymmetric bonding mode becoming increasingly more dominant for longer wavelengths. These findings are consistent with the spectra and spatial distributions in Figs. 3(a) and 3(b). We note that the excitation positions near the apex are more relevant for the overall response as the CL and EELS intensity is highest at those positions [see EELS and CL maps in Fig. 2(f)]. Hence, we conclude that the main peak in the average spectrum shown in Fig. 2(d) indeed is a mixture of two modes, illustrating that spectra of such coupled structures have to be carefully interpreted.

IV. SIZE-DEPENDENT OPTICAL RESPONSE

Having understood the individual dolmen elements we now move to the dolmen structures. Previously, we have focused on the coupling between elements in the dolmen and how this is affected by the electron impact position [33]. Here, we investigate how the dolmen response scales with size. It is well known that plasmonic resonances generally redshift for increasing particle size. Figure 4(a) shows EELS and CL spectra taken at position **A** [excitation of the horizontal monomer; see Fig. 1(a)] for the three fabricated dolmen sizes (see Table III for peak positions and amplitudes). For the smallest dolmen we observe two peaks and for the larger dolmens we see that an extra peak appears in the blue part of the spectrum. This additional peak can be attributed to the transverse monomer resonance also shown in Figs. 2(a) and 2(b). Strictly speaking, this monomer resonance can also hybridize with the dimer but the coupling is too weak to
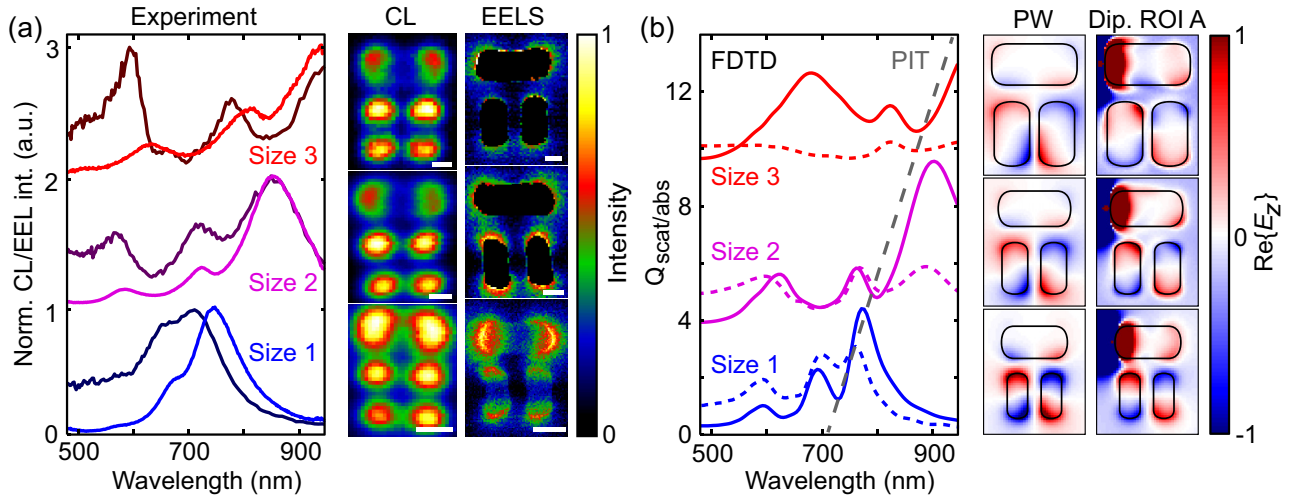

FIG. 4. (a) EELS (dark curves) and CL spectra (light curves) at excitation position 1 for all dolmen sizes. The spectra have been vertically offset for clarity. The peak amplitudes and positions are listed in Table III. The EELS and CL spatial maps in the spectral region between bonding and antibonding mode where the PIT window occurs are shown on the right (at $\lambda_0 = 685$, 755, and 840 nm for sizes 1, 2, and 3, respectively). Scale bars correspond to 50 nm. (b) Normalized scattering (solid curves) and absorption (dashed curves) cross sections of dolmen structures for polarization along the top bar, calculated by FDTD. The spectra have again been vertically offset for clarity. The PIT feature indicated by the gray dashed line shifts with size toward the red. First column on the right shows the E_z near-field distribution at the PIT window for plane-wave excitation (PW) ($\lambda_0 = 730$, 750, and 880 nm for sizes 1, 2, and 3, respectively). Second column shows the same maps for vertical point dipole excitation 10 nm left of the top bar (excitation position **A**) at half-height of the rod.

TABLE III. Peak amplitudes and center wavelengths (in between brackets) for the normalized CL and EELS spectra of the three dolmen sizes [Fig. 4(a)]. For the largest dolmen (size 3) the CL measurement does not extend far enough into the IR to record the actual peak center wavelength for peak 3. The wavelength only indicates the limit of the detection range in this case. In EELS the peak position was properly resolved because the measurement extends all the way to the zero-loss peak (not shown here).

	CL	EELS
Size 1/peak 1	0.47 (672 nm)	0.87 (656 nm)
Size 1/peak 2	1 (750 nm)	1 (712 nm)
Size 2/peak 1	0.15 (582 nm)	0.55 (568 nm)
Size 2/peak 2	0.32 (724 nm)	0.66 (720 nm)
Size 2/peak 3	1 (857 nm)	1 (855 nm)
Size 3/peak 1	0.26 (630 nm)	1 (593 nm)
Size 3/peak 2	0.51 (807 nm)	0.71 (780 nm)
Size 3/peak 3	1 (935 nm*)	0.90 (953 nm)

observe a perturbation. This transverse monomer mode is too strongly damped in the case of the small dolmens to give a significant EELS and CL response. The other two peaks correspond to the antibonding (central peak) and bonding modes (right peak) of the dolmen, respectively [see Fig. 1(f) for charge distributions]. For these modes there is a stronger interaction between the dimer and monomer, which is why both hybrid modes are visible, even though only the monomer is being driven directly (see Ref. [33] for a more detailed description of this coupling behavior in the dolmen). This dimer-monomer coupling behavior is clearly preserved with dolmen size. Additionally, all of the modes move toward the red as the size increases, although the exact detuning between the peaks varies somewhat for each size. This redshift is also observed in the spectra for the dimer excitation positions (not shown here). Such redshifting for increasingly larger structures is generally observed in plasmonic systems and can be explained by the increase in phase retardation across the structure [1]. On the right side of the figure we also show the EELS and CL excitation maps for the spectral point between the antibonding and bonding mode at $\lambda_0 = 685$, 755, and 840 nm for size 1, 2, and 3, respectively. Similar to the spectra, the spatial profiles do not change significantly as the size increases. For the smallest size dolmen the excitation positions on the particles were not masked in the EELS spatial maps because the metal is substantially thinner (33 nm instead of 40 nm; see Table I) and the EELS signal better reflects the optical modes that are excited because of a strong reduction in the inelastic contributions.

For the smallest dolmens the CL data is significantly redshifted compared to the EELS data. The redshift in the CL experiments is due to the local deposition of a thin carbonaceous contamination layer during electron beam scanning which we only observed on this specific sample. Despite the redshifting the quality factors and spectral shape remained roughly constant, which means that we can still qualitatively compare the spectral shapes for EELS and CL. The spectral shape of the EELS spectrum for this size differs clearly from the CL, which shows that the total response (measured with EELS) differs from the purely radiative response (measured with CL).

For sizes 2 and 3 the responses are more similar, although in the EELS spectra the features at higher energies are more pronounced, similar to the reference structures (see Fig. 2).

Figure 4(b) shows the plane-wave scattering and absorption cross section for horizontal polarization along the monomer for each of the dolmen sizes, calculated using FDTD. This allows us to study the similarities and differences between plane-wave and electron beam excitation. Also in the plane-wave response the spectral features redshift for increasing size, and we see that the scattering to absorption ratio is smallest for the smallest dolmen size as expected, which could possibly explain the larger discrepancy between the EELS and CL spectral shape for this size. Furthermore, we observe a modest transparency window for each size (indicated by the gray dashed line). If one decreases the dimer-monomer spacing d to below 30 nm the FDTD spectra show that the modal splitting and modulation depth of the window can be substantially increased (not shown here). To prove that this transparency window is similar to those discussed in literature we show the induced E_z near-field distribution at the PIT wavelength, for each of the sizes in the first column on the right of Fig. 4(b). We clearly see the reduced intensity on the monomer and the antisymmetric field distribution in the dimer. To demonstrate that the well-known hybrid dolmen modes can also be driven when locally excited by a point-like source we show the near-field patterns for dipole excitation at excitation position **A** as well [see second column in Fig. 4(b)]. We can clearly recognize the characteristic antisymmetric dimer mode in all dolmen sizes, showing that this type of local driving indeed leads to the excitation of the same modes as for horizontally polarized plane-wave excitation, independent of the size of the dolmen. Although we observe coupling effects in the measurements, the system is not coupled strongly enough to display highly dispersive features such as a distinct Fano lineshape or PIT window. We note that in the plane-wave simulations the transverse mode in the dimer is driven simultaneously which leads to an increased contributions around $\lambda_0 = 600$, 640, and 680 nm for size 1, 2, and 3, respectively. As mentioned previously, however, the high-energy peak in the EELS and CL responses is related to the transverse monomer mode (the transverse dimer mode is not excited at **A**) and therefore cannot be compared with these peaks in FDTD. The two low-energy peaks of the FDTD spectra can be compared to the experiments more directly because they correspond to the same modes. Especially for the largest two dolmens there is a good qualitative correspondence to the red part of the FDTD spectra.

V. VARYING INTRINSIC COUPLING STRENGTH

So far we have investigated the effect of size on the optical response of the dolmen geometry. Next, we control the degree of intrinsic coupling between the dolmen elements. The coupling between monomer and dimer is mediated by the induced near fields in the nanorods, which extend ∼30 nm away from the structure. Hence, the intrinsic coupling strength is mainly determined by the spacing d between monomer and dimer. Figures 5(a) and 5(b) show CL and EELS spectra at positions **A** and **B** for dolmens of size 1 with different spacings $d = 30$, 40, 50, and 60 nm. We have also included reference spectra from an individual reference monomer and dimer of
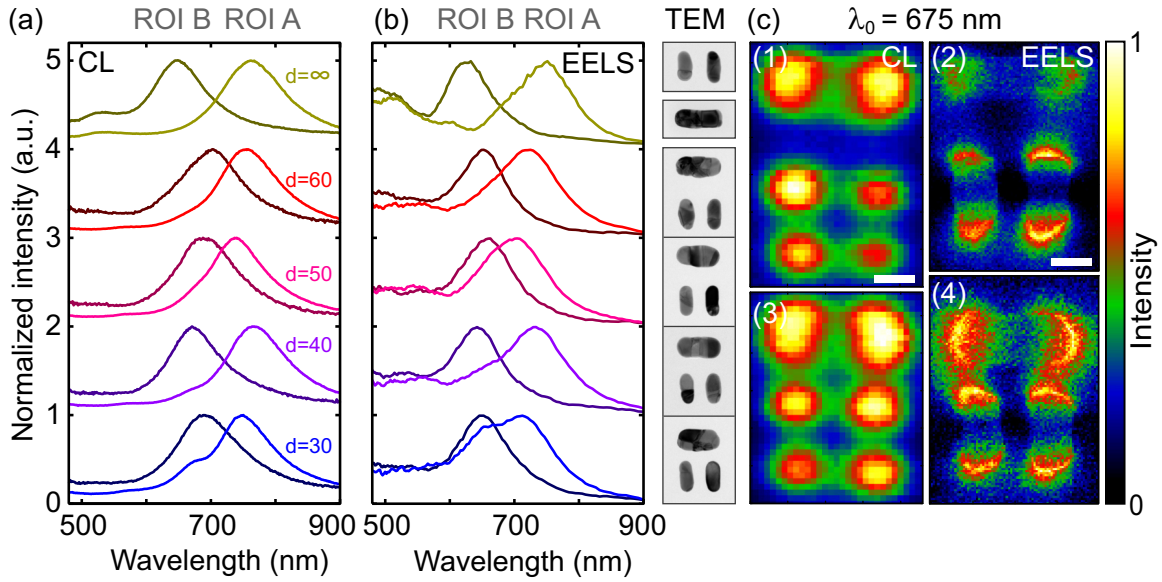
FIG. 5. Change in coupling as function of distance d between top bar and dimer. (a) CL spectra and (b) EELS spectra for positions **A** and **B** for dolmen size 1 at spacings $d = 30$, 40, 50, and 60 nm. We also show the reference single bar and dimer spectra ($d = \infty$). The spectra have been vertically offset for clarity. On the right side we show the corresponding BF TEM images of the structures. (c) CL (maps 1 and 3) and EELS (maps 2 and 4) maps for $d = 30$ and $d = 60$ nm at $\lambda_0 = 675$ nm. Scale bars correspond to 50 nm.

this size ("$d = \infty$"). The spectra are vertically offset for clarity. For each separation distance the corresponding BF TEM image is shown on the right.

As described in detail in Ref. [33], the coupling between monomer and dimer is most clearly reflected in the fact that both the bonding and antibonding hybrid dolmen modes are visible in the EELS and CL spectra for excitation at **A**. For the dolmen size considered in Fig. 5, the main peak centered around $\lambda_0 = 750$ nm corresponds to the bonding mode and the antibonding mode is visible as a shoulder at $\lambda_0 = 675$ nm (for the smallest spacing of $d = 30$ nm). For $d = 40$ nm this shoulder is substantially lower and disappears completely for the dolmens with larger particle spacings, where the spectrum just resembles the spectrum of an isolated monomer, indicating that the dimer and monomer mode no longer couple and act as independent resonators. These results show that efficient near-field coupling between dimer and monomer requires spacings smaller than 40 nm for this dolmen size. The spectra for position **B** do not noticeably change as the distance between the elements increases and are close to the isolated dimer spectrum. For this excitation position a smaller effect of the coupling on the spectrum is expected [33]. We note that the main resonance positions also vary slightly from dolmen to dolmen without a clear trend, which we attribute to small size and shape variations in the dolmen elements. Figure 5(c) shows CL and EELS maps for $\lambda_0 = 675$ nm for $d = 60$ nm (maps 1 and 2) and $d = 30$ nm (maps 3 and 4). These profiles reveal that there is significant field overlap between monomer and dimer in the case of $d = 30$, reflecting the efficient near-field coupling, while for $d = 60$ nm this overlap is much lower thereby preventing effective coupling between dimer and monomer. As a result of this difference in coupling efficiency the EELS intensity and CL intensity measured on the monomer at $\lambda_0 = 675$ nm is reduced for larger spacings. This effect is particularly clear in the EELS maps 2 and 4.

These results demonstrate that near-field coupling can affect the spectral shape as well as the spatial profile of CL and EELS measurements and that such coupling can be studied in detail using these techniques.

VI. CONCLUSIONS

In conclusion, we have studied the resulting electron energy-loss and cathodoluminescence emission when a beam of fast electrons is used to excite individual or coupled metallic nanorods placed in a dimer or dolmen metamolecule configuration. We directly compare electron energy-loss and cathodoluminescence signals and determine the radiative properties of the plasmonic modes with deep-subwavelength resolution. We find that the electron energy-loss response is stronger for higher energies compared to the cathodoluminescence spectra, related to the far-field scattering efficiency of these modes. The transverse antibonding dimer mode, in particular, is so heavily damped that it only shows up in the electron energy-loss spectrum. We demonstrate that the dolmen spectral response redshifts for increasing size as is expected for plasmonic structures. The dimer-monomer coupling that is observed in the dolmen spectra is a nanoscale near-field effect and we show that the intrinsic coupling can be reduced by increasing the spacing between the elements. We show that this coupling has a pronounced effect on the spectra and observed spatial excitation profiles. This work demonstrates that combining electron energy-loss and cathodoluminescence spectroscopy provides a powerful method to elucidate the optical properties of complex nanophotonic systems at the nanoscale.

[1] N. J. Halas, S. Lal, W. Chang, S. Link, and P. Nordlander, Chem. Rev. **111**, 3913 (2011).

[2] L. Novotny and N. van Hulst, Nat. Photon. **5**, 83 (2011).

[3] M. Notomi, Rep. Prog. Phys. **73**, 096501 (2010).

[4] J. A. Schuller, E. S. Barnard, W. Cai, Y. C. Jun, J. White, and M. L. Brongersma, Nat. Mater. **9**, 193 (2010).

[5] H. A. Atwater and A. Polman, Nat. Mater. **9**, 205 (2010).

[6] F. J. García de Abajo, Rev. Mod. Phys. **82**, 209 (2010).

[7] T. Coenen, E. J. R. Vesseur, A. Polman, and A. F. Koenderink, Nano Lett. **11**, 3779 (2011).

[8] N. Yamamoto, S. Ohtani, and F. J. García de Abajo, Nano Lett. **11**, 91 (2011).

[9] X. Zhu, J. Zhang, J. Xu, H. Li, X. Wu, Z. Liao, Q. Zhao, and D. P. Yu, ACS Nano **5**, 6546 (2011).

[10] R. Sapienza, T. Coenen, J. Renger, M. Kuttge, N. F. van Hulst, and A. Polman, Nat. Mater. **11**, 781 (2012).

[11] A. C. Atre, B. J. M. Brenny, T. Coenen, A. Polman, A. García-Etxarri, and J. A. Dionne, Nat. Nanotechnol. **10**, 429 (2015).

[12] J. Nelayah, M. Kociak, O. Stéphan, F. J. García de Abajo, M. Tencé, L. Henrard, D. Taverna, I. Pastoriza-Santos, L. M. Liz-Marzán, and C. Colliex, Nat. Phys. **3**, 348 (2007).

[13] D. Rossouw, V. J. Couillard, E. Kumacheva, and G. A. Botton, Nano Lett. **11**, 1499 (2011).

[14] S. von Cube, F. Irsen, R. Diehl, J. Niegemann, K. Busch, and S. Linden, Nano Lett. **13**, 703 (2012).

[15] O. Nicoletti, F. de la Peña, R. K. Leary, D. J. Holland, C. Ducati, and P. A. Midgley, Nature **502**, 80 (2013).

[16] F.-P. Schmidt, H. Ditlbacher, U. Hohenester, A. Hohenau, F. Hofer, and J. R. Krenn, Nat. Commun. **5**, 3604 (2014).

[17] S. Barrow, D. Rossouw, A. M. Funston, G. A. Botton, and P. Mulvaney, Nano Lett. **14**, 3799 (2014).

[18] S. F. Tan, L. Wu, J. K. W. Yang, P. Bai, M. Bosman, and C. A. Nijhuis, Science **343**, 1496 (2014).

[19] C. Colliex, O. Stéphan, and M. Kociak, Ultramicroscopy **162**, A1 (2015).

[20] A. Teulle, M. Bosman, C. Girard, K. L. Gurunatha, M. Li, S. Mann, and E. Erik Dujardin, Nat. Mater. **14**, 87 (2014).

[21] M. Bosman, V. J. Keast, J. L. García-Muñoz, A. J. D'Alfonso, S. D. Findlay, and L. J. Allen, Phys. Rev. Lett. **99**, 086102 (2007).

[22] Z. Mahfoud, A. T. Dijksman, C. Javaux, P. Bassoul, A. L. Baudrion, J. Plain, B. Dubertret, and M. Kociak, J. Phys. Chem. Lett. **4**, 4090 (2013).

[23] A. Losquin and M. Kociak, ACS Photonics **2**, 1619 (2015).

[24] S. Zhang, D. A. Genov, Y. Wang, M. Liu, and X. Zhang, Phys. Rev. Lett. **101**, 047401 (2008).

[25] N. Verellen, Y. Sonnefraud, H. Sobhani, F. Hao, V. V. Moshchalkov, P. Van Dorpe, P. Nordlander, and S. A. Maier, Nano Lett. **9**, 1663 (2009).

[26] N. Liu, L. Langguth, T. Weiss, J. Kästel, M. Fleischhauer, T. Pfau, and H. Giessen, Nat. Mater. **8**, 758 (2009).

[27] S.-O. Guillaume, N. Geuquet, and L. Henrard, Proc. SPIE **8096**, 80962E (2011).

[28] Z. Ye, S. Zhang, Y. Wang, Y.-S. Park, T. Zentgraf, G. Bartal, X. Yin, and X. Zhang, Phys. Rev. B **86**, 155148 (2012).

[29] C. Forestiere, L. Dal Negro, and G. Miano, Phys. Rev. B **88**, 155411 (2013).

[30] B. Abasahl, C. Santschi, and O. J. F. Martin, ACS Photonics **1**, 403 (2014).

[31] C. Yan and O. J. F. Martin, ACS Nano **8**, 11860 (2014).

[32] FDTD solutions, Lumerical Solutions Inc., www.lumerical.com.

[33] T. Coenen, D. T. Schoen, S. Mann, S. R. K. Rodriguez, B. J. M. Brenny, A. Polman, and M. L. Brongersma, Nano Lett. **15**, 7666 (2015).

[34] T. Coenen, E. J. R. Vesseur, and A. Polman, Appl. Phys. Lett. **99**, 143103 (2011).

[35] A. Arbouet, A. Mlayah, G. Christian, and G. Colas des Francs, New J. Phys. **16**, 113012 (2014).

[36] K. Busch, M. König, and J. Niegemann, Laser Photonics Rev. **5**, 773 (2011).

[37] F. J. García de Abajo and A. Howie, Phys. Rev. Lett. **80**, 5180 (1998).

[38] U. Hohenester, H. Ditlbacher, and J. R. Krenn, Phys. Rev. Lett. **103**, 106801 (2009).

[39] N. W. Bigelow, A. Vaschillo, V. Iberi, J. P. Camden, and D. J. Masiello, ACS Nano **6**, 7497 (2012).

[40] P. Das, T. K. Chini, and J. Pond, J. Phys. Chem. C **116**, 15610 (2012).

[41] J. Zuloaga and P. Nordlander, Nano Lett. **11**, 1280 (2011).

[42] V. Myroshnychenko, J. Nelayah, G. Adamo, N. Geuquet, J. Rodríguez-Fernández, I. Pastoriza-Santos, K. F. MacDonald, L. Henrard, L. M. Liz-Marzán, N. I. Zheludev, M. Kociak, and F. J. García de Abajo, Nano Lett. **12**, 4172 (2012).

[43] M. Husnik, F. von Cube, S. Irsen, S. Linden, S. J. Niegemann, K. Busch, and M. Wegener, Nanophotonics **2**, 241 (2013).

[44] M. W. Chu, V. Myroshnychenko, C. H. Chen, J. P. Deng, C. Y. Mou, and F. J. García de Abajo, Nano Lett. **9**, 399 (2009).

[45] T. Coenen, E. J. R. Vesseur, and A. Polman, ACS Nano **6**, 1742 (2012).

[46] E. Prodan, C. Radloff, N. J. Halas, and P. Nordlander, Science **302**, 419 (2003).

[47] P. Nordlander, C. Oubre, E. Prodan, K. Li, and M. I. Stockman, Nano Lett. **4**, 899 (2004).

[48] S. C. Yang, H. Kobori, C. L. He, M. E. Lin, H. Y. Chen, C. Li, M. Kanehara, T. Teranishi, and S. Gwo, Nano Lett. **10**, 632 (2010).

[49] J. Kern, S. Großmann, N. V. Tarakina, T. Háckel, M. Emmerling, M. Kamp, J. S. Huang, P. Biagioni, J. C. Prangsma, and B. Hecht, Nano Lett. **12**, 5504 (2012).

[50] P. Pablo Alonso-González, P. Albella, F. Golmar, L. Arzubiaga, F. Casanova, L. E. Hueso, J. Aizpurua, and R. Hillenbrand, Opt. Express **21**, 1270 (2013).

[51] F. Bernal Arango, T. Coenen, and A. F. Koenderink, ACS Photon. **1**, 444 (2014).

[52] A. L. Koh, K. Bao, I. Khan, W. E. Smith, G. Kothleitner, P. Nordlander, S. A. Maier, and D. W. McComb, ACS Nano **3**, 3015 (2009).

[53] I. Alber, W. Sigle, S. Müller, R. Neumann, O. Picht, M. Rauber, P. A. van Aken, and M. A. Toimil-Molares, ACS Nano **5**, 9845 (2011).

[54] K. H. Fung, A. Kumar, and N. X. Fang, Phys. Rev. B **89**, 045408 (2014).